Multilayered Kelvin–Helmholtz Instability in the Solar Corona

Ding Yuan[1,2,8] , Yuandeng Shen[3,8] , Yu Liu[3] , Hongbo Li[4] , Xueshang Feng[1] , and Rony Keppens[5,6,7]

[1] Institute of Space Science and Applied Technology, Harbin Institute of Technology, Shenzhen 518055, People's Republic of China; yuanding@hit.edu.cn, ydshen@ynao.ac.cn

[2] Key Laboratory of Solar Activity, National Astronomical Observatories, Chinese Academy of Sciences, Beijing 100012, People's Republic of China

[3] Yunnan Astronomical Observatory, Chinese Academy of Sciences, P.O. Box 110, Kunming 650011, People's Republic of China

[4] Institute of Space Physics, Luoyang Normal University, Luoyang 471934, People's Republic of China

[5] Centre for mathematical Plasma Astrophysics, Department of Mathematics, KU Leuven, Celestijnenlaan 200B, Leuven 3001, Belgium

[6] School of Astronomy and Space Science, Nanjing University, Nanjing 210023, People's Republic of China

[7] Purple Mountain Observatory, Chinese Academy of Sciences, Nanjing 210023, People's Republic of China

Abstract

The Kelvin–Helmholtz (KH) instability is commonly found in many astrophysical, laboratory, and space plasmas. It could mix plasma components of different properties and convert dynamic fluid energy from large-scale structure to smaller ones. In this study, we combined the ground-based New Vacuum Solar Telescope (NVST) and the *Solar Dynamic Observatories*/Atmospheric Imaging Assembly (AIA) to observe the plasma dynamics associated with active region 12673 on 2017 September 9. In this multitemperature view, we identified three adjacent layers of plasma flowing at different speeds, and detected KH instabilities at their interfaces. We could unambiguously track a typical KH vortex and measure its motion. We found that the speed of this vortex suddenly tripled at a certain stage. This acceleration was synchronized with the enhancements in emission measure and average intensity of the 193 Å data. We interpret this as evidence that KH instability triggers plasma heating. The intriguing feature in this event is that the KH instability observed in the NVST channel was nearly complementary to that in the AIA 193 Å. Such a multithermal energy exchange process is easily overlooked in previous studies, as the cold plasma component is usually not visible in the extreme-ultraviolet channels that are only sensitive to high-temperature plasma emissions. Our finding indicates that embedded cold layers could interact with hot plasma as invisible matters. We speculate that this process could occur at a variety of length scales and could contribute to plasma heating.

Key words: instabilities – magnetohydrodynamics (MHD) – Sun: atmosphere – Sun: corona

Supporting material: animation

1. Introduction

The Kelvin–Helmholtz (KH) instabilities can occur in any fluid or plasma with a continuous velocity shear or at the interface of two shearing fluids with different density or temperature (Thomson 1871; von Helmholtz 1868). However, in a magnetized plasma, compressibility and magnetic tension could have a stabilizing effect on the instabilities. Hence, the velocity shear has to reach a threshold to grow into instability (Chandrasekhar 1961).

The KH instability is an important mechanism in the evolution of turbulence in the stratified interior of the ocean (e.g., Smyth & Moum 2012) and in the atmosphere of the Earth and giant planets, e.g., Jupiter, Saturn (e.g., Houze 2014). KH instability is also detected in collisionless space plasmas throughout the solar system, for instance, at the magnetopause of the Earth, Mercury, Jupiter, and Saturn (e.g., Johnson et al. 2014), and in many space and astrophysical plasmas (e.g., Murray et al. 1993; Vietri et al. 1997; Lobanov & Zensus 2001; Wang & Chevalier 2001; Bucciantini et al. 2005; Berné et al. 2010).

In the solar atmosphere, KH instability is observed at a variety of scales, e.g., as growing ripples at the interface between a prominence and the corona (Ryutova et al. 2010; Berger et al. 2017; Hillier & Polito 2018; Yang et al. 2018). KH and other plasma instabilities are believed to be the key

processes in dispersing and evaporating cool prominence material into the hot corona (Berger et al. 2017; Hillier & Polito 2018; Li et al. 2018a). Ofman & Thompson (2011) reported the growth and saturation of KH vortices at the interface between erupting and nonerupting plasmas during a coronal material ejection (CME) event. Similar KH vortices were observed at the flank of an erupting CME (Foullon et al. 2011) and coronal streamers (Feng et al. 2013).

In high-temperature plasma, field-aligned conductivity is very large (Braginskii 1965), and the charged particles are frozen in the magnetic field lines, i.e., the plasma expands and contracts with conserved magnetic flux. In typical low β coronal plasma, strong magnetization ensures that plasma could stream freely along the magnetic field lines, so we expect any velocity gradient would form preferentially across the magnetic field. Li et al. (2018b) reported plasma temperature enhancement after KH instability in coronal loops. It implies that KH instability could trigger plasma heating. This process was elucidated by nonlinear magnetohydrodynamic (MHD) simulations (e.g., Fang et al. 2016). Recently, Ruan et al. (2018) simulated the growth of KH instability in post-flare loop, which was invaded by evaporation flows. Loop-top soft and hard X-ray emission sources were predicted. KH vortices thereby grow into a highly nonlinear stage and roll up the magnetic field lines. Magnetic islands are formed and release energy by magnetic reconnection (Fang et al. 2016; Ruan et al. 2018).

In this study, we report the observation of multithermal layers that interact with one another by means of KH

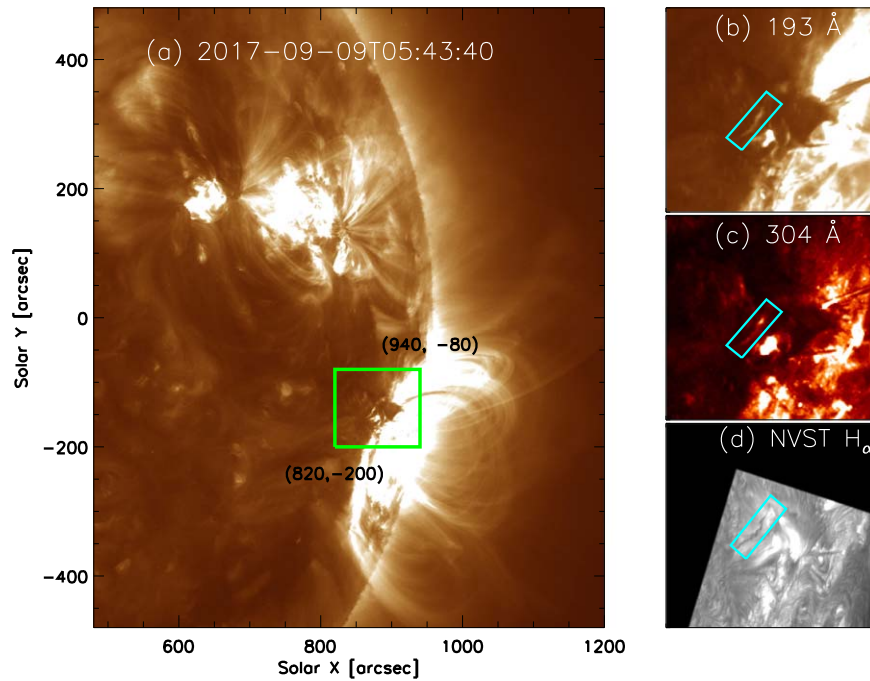[8] These authors contribute equally to this work.

Figure 1. (a) Field of view of the AIA 193 Å channel showing the plasma motion on the northeast outskirt of AR 12673. (b)–(d) Highlights of the region of interest (the green box in panel (a)) in the 193 Å, 304 Å, and NVST H$_\alpha$ images, respectively. The areas enclosed by the tilted rectangles are erected in Figure 2 to visualize the plasma motion. An animation of the 193 Å, 304 Å, and NVST H$_\alpha$ images is available. The area in the tilted rectangles in 193 Å and H$_\alpha$ is also animated to show the plasma flow evolution. The entire animation runs from to 05:00 to 06:30 UT.

(An animation of this figure is available.)

instability. The interaction between cool and hot plasma sheets results in localized temperature enhancements and acceleration of bulk plasma. The observation and method are given in Section 2; the results are presented in Section 3; then we proceed to discussions and conclusions in Section 4.

2. Observation and Data Analysis

A GOES class M1.1 flare was observed at the active region (AR) 12673 on 2017 September 9 by the Atmospheric Imaging Assembly (AIA; Lemen et al. 2012) on board the *Solar Dynamics Observatories* (*SDO*). This flare was triggered on 04:14:00 UT and stopped on 04:43:00 UT. The New Vacuum Solar Telescope (NVST; Liu et al. 2014) operated between 05:34:14 UT and 06:07:30 UT, so it only recorded the relaxation stage of the flare. A bulk of plasma erupted after the flare. In the meantime, magnetic field lines relaxed from intertwinement. A filament-like plasma sheet was left over, presumably being supported by the relaxed magnetic field, which appears to extend radially into outer space (see Figure 1(a)). This plasma sheet moved horizontally across the dominant magnetic field, and developed a chain of kink displacements in a snake-like shape (see Figures 1(b)–(c)).

Our observation was made with the ground-based high-resolution NVST and *SDO*/AIA. In NVST's operation, the H$_\alpha$ Lyot filter was tuned to the line center ($\lambda = 6562.8$ Å) for fast imaging. This narrowband filter was optimized to record plasma emissions at about 10,000 K. The filter's bandwidth is about 0.25 Å; each image was recorded with an exposure time of about 20 ms. The sampling interval was about 5 s, and the spatial resolution 0$\overset{''}{.}$262 or about 190 km. *SDO*/AIA took extreme-ultraviolet (EUV) images about every 12 s with a spatial resolution of about 1$\overset{''}{.}$2. AIA EUV filters was optimized

to record the emissions of hot plasma with temperature ranging from 50,000 to 20,000,000 K.

We processed the NVST H$_\alpha$ images by removing the dark current and normalizing them with a flat field. Then, we applied a lucky imaging algorithm to the data. Finally, the NVST images were rotated to align with the solar north and translated to match the key features recorded in the AIA 304 Å channel (see Figure 1(c)). The AIA images were calibrated with the standard processing routines available in the solar software library (Freeland & Handy 1998).

We combined multiwavelength EUV imaging data recorded by *SDO*/AIA: 94, 131, 171, 193, 211, and 335 Å, and used a regularized inversion method (Hannah & Kontar 2012) to recover the differential emission measure (DEM). The DEM of a coronal element normally varies with temperature in a Gaussian profile (Del Zanna et al. 2015); therefore, the plasma temperature can be estimated as the value where the DEM reaches its maximum. The emission measure (EM) was calculated by integrating DEM over temperature. The EM is proportional to the electron density squared, i.e., EM $= 0.83 h n_e^2$, where h is the column depth, n_e is the number density of electron, and the factor of 0.83 arises from accounting for the contribution of the ionized helium electrons.

In order to study the evolution of the instability, we traced a blob of plasma; its positions are marked in Figure 2(c). We used the pixel with maximum emission intensity within each box as the barycenter; the tracking error was estimated to be 1 AIA pixel. We spotted the difference in propagation speed before and after 05:43:12 UT (time stamp 4), so we used two linear fits to obtain the speeds; the result is illustrated in Figure 3(a).
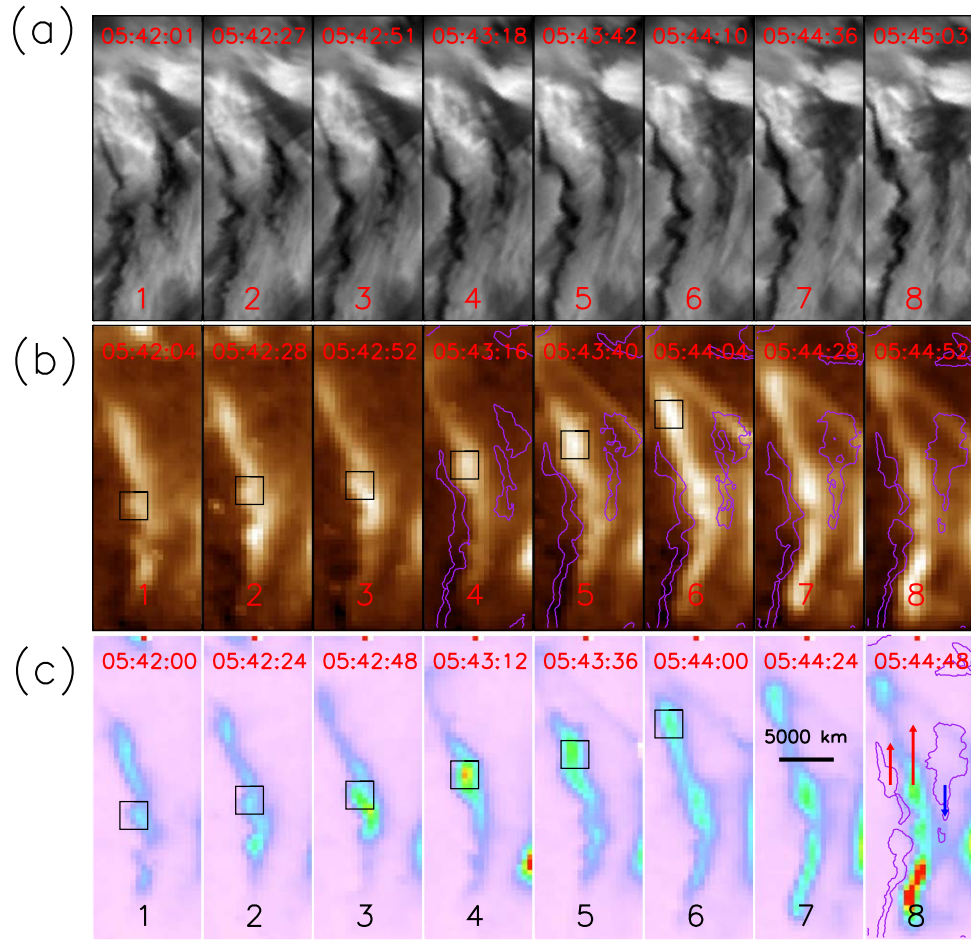
Figure 2. (a) Plasma flow evolution observed by the NVST H_α channel. (b) Coronal flow component observed by the AIA 193 Å channel. The contours overlaid in the fourth–eighth snapshots are based on the NVST H_α emission intensities displayed in panel (a). It shows that boundaries of the coronal and chromospheric flow components complement each other at the contact surface. (c) DEM at $T = 1250,000$ K. Uniform time stamps of 1–8 are allocated to each snapshot, although the measurements for each instrument are taken at slightly shifted times. The contours and arrows plotted in the eighth frame in panel (c) give the relative motions of the plasma material; the lengths of the arrows are scaled with the speed value, i.e., 28 km s^{-1}, 40 km s^{-1} ,and -21 km s^{-1}, respectively. An animation of panels (a) and (b) is provided in Figure 1.

3. Results

3.1. Parameters for the KH Instability

The KH instability initially developed as a kink displacement of the plasma filament, as observed in most AIA channels and in detail by the NVST H_α channel. The difference between a stable wave and a linear KH instability relies on whether the growth rate of wave amplitude is zero or positive. In our case, the wave amplitude grew. The wavelength was about 2 Mm. NVST revealed the fine detail of the kink motion: the wavelength varied from 1 Mm to 2.5 Mm along the spine of the filament (Figure 2). The vortices also varied in size from less than 1 Mm to about 2 Mm. The propagation speed was about 30 km s^{-1}.

3.2. Multilayered KH Instability

Two flow components were observed in the NVST H_α channel (Figure 2(a)). They propagated toward opposite directions; the projected propagation speeds were about 28 km s^{-1} and -21 km s^{-1}, respectively. These two flows were separated by a layer of invisible material (Figure 2(a)). We plot the contour of H_α emission over the 193 Å images in Figure 2(b). It reveals that the flow component in the 193 Å

channel fills up the gap; the projected propagation speed of this layer was about 40 km s^{-1}. A remarkable feature is that kink displacements associated with the KH instability in H_α channel were complementary to the counterpart in the 193 Å channel; see Figure 2(b). It indicates that these three flows captured at different channels were adjacent layers of shearing plasma. This scenario is depicted in the eighth panel of Figure 2(c).

3.3. Onset and Growth of the KH Instability

AR 12673 had rotated to the limb, so we could not obtain the coronal magnetic field by extrapolation. The onset condition of the KH instability at the contact surface of two bulk plasmas is (Chandrasekhar 1961)

$$[\boldsymbol{k} \cdot \Delta \boldsymbol{v}]^2 > \frac{\rho_1 + \rho_2}{\mu_0 \rho_1 \rho_2}[(\boldsymbol{k} \cdot \boldsymbol{B}_1)^2 + (\boldsymbol{k} \cdot \boldsymbol{B}_2)^2], \qquad (1)$$

where $\boldsymbol{k} = 2\pi/\lambda$ is the wave vector, λ is the wavelength, $\Delta \boldsymbol{v}$ is the velocity difference, ρ_1 and ρ_2 are the respective density of two layers, $\boldsymbol{B}_1$ and $\boldsymbol{B}_2$ are the magnetic field vectors in two plasma layers, and μ_0 is the magnetic permeability in free space. For simplicity, we assume that the magnetic field is the same in two plasmas, i.e., $\boldsymbol{B}_2 = \boldsymbol{B}_1$. The onset condition gives
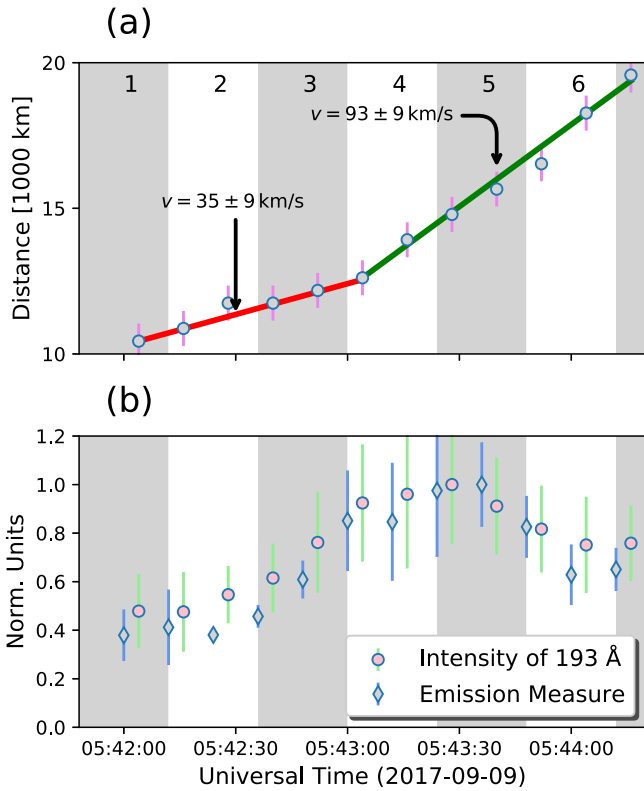
(a)

(b)

Figure 3. (a) Position of the plasma blob traced in Figure 2. (b) Average emission intensity in the AIA 193 Å channel and the EM. The time stamps correspond to those labeled in Figure 2.

an upper limit for the parallel magnetic component

$$B_\parallel < \frac{\Delta v \sqrt{\mu_0 \rho_2 \rho_1}}{\sqrt{2(\rho_2 + \rho_1)}} = 0.8 \text{ G.} \qquad (2)$$

Here we have used a density ratio $\rho_2/\rho_1 = 10$ in this estimation. The $B_\parallel$ obtained here is only a fraction of typical coronal magnetic field strength. However, we note there are a number of factors that we have not considered: (1) Chandrasekhar (1961) assumes the KH instability grows from a small-amplitude linear perturbation to a sharp contact interface and uses incompressible conditions. In real observation, the deformed vortices could well violate first-order perturbation. We may have measured the nonlinear stage of KH instability. (2) A real plasma involves extra physical terms other than ideal MHD, e.g., viscosity, thermal conduction, partial ionization, heating, etc.

3.4. Heating Effect

We traced a vortex structure within a 5×5 macro pixel as labeled in Figure 2(b), and measured its position, averaged emission intensity, and EM. The EM was measured to be $3.7^{\pm1.8} \times 10^{27}$ cm^{-5}, and the temperature $1.5^{\pm0.5} \times 10^6$ K. If we assume that the column depth was about 3–5 pixels, namely, $h = 1.8^{\pm0.6} \times 10^6$ m, then the number density of electrons was estimated with $n_e = \sqrt{EM/0.83h} = 5.0^{\pm1.5} \times 10^{10}$ cm^{-3} (also see Aschwanden et al. 2013). This blob of material had a plasma density at the level of flaring loops (Huang et al. 2018).

The center of this vortex migrated at a speed of about $35^{\pm9}$ km s^{-1} and suddenly almost tripled to about $93^{\pm9}$ km s^{-1} at 05:43:00 UT (Figure 3(a)). In the meantime, the emission intensity and EM reached their maximums (Figure 3(b)). It is evident that the sudden jump in propagation speed was a response to localized plasma heating, which was likely to be triggered by the KH instability.

If we assume that the energy deposition was constrained within an area $A = \pi D^2/4$, and D was estimated as 3 AIA pixels (about 1500 km), and that it was released within $\delta t = 12$ s, the dynamic energy gained by the plasma vortex was estimated as $\delta E = \delta q A \delta t$, where $q = 1/2\rho v^3$ is the energy density flux of dynamic energy in a directional flow. In this case, we assume the inflow and outflow had speeds of 35 km s^{-1} and 93 km s^{-1}, respectively (see Figure 3(a)), and the density remained constant over the course. So the dynamic energy gained during this acceleration was about 5.0×10^{17} Joule. This is about 2–3 orders of magnitude smaller than a detectable flare, but 2–5 orders of magnitude greater than a nanoflare (Klimchuk 2006). Sudden energy relaxation impulsively heated the local plasma to high temperature, and resulted in a sudden jump of local gas pressure, which then caused quick expansion and acceleration of local plasma.

4. Discussions and Conclusion

In this study, we observed that multiple adjacent layers with significant density and temperature contrasts flowed with a velocity shear, and found that KH instabilities grew at their contact surfaces. The sudden jerk of a plasma vortex was synchronized with the enhancements for emission measure of the plasma and the emission intensity of the 193 Å channel. It implies that a sudden energy release may have occurred at that time.

The uniqueness of this event is that if one uses a single narrowband channel that is sensitive to hot plasma emission, one would intuitively neglect the interaction with cold plasma, and vice versa. However, we show in this multi-instrument study, cold plasma interacts with coronal plasma as invisible matter, and bolsters mass and energy exchanges.

This sort of event cannot be observed with a single narrowband channel. However, shearing motions are very common in the solar atmosphere and should occur at a vast range of scales. The dark features in the EUV images are intuitively considered as "vacuum," and therefore are usually neglected. A positive example is that the dark small-scale filament eruption is found as the driver for X-ray jets and revised the jet eruption model (Shen et al. 2012, 2017; Sterling et al. 2015). De Pontieu et al. (2011) similarly raise the importance of heating by type II spicules at the interface of photospheric and coronal material. As the corona is very inhomogeneous and is filled with dark features at a variety of scales, the induced interaction between hot and cold plasmas could play a significant role in energy dissipation throughout the solar corona.

KH instability and its associated secondary effects could be well observed in space plasmas. During a coronal mass ejection, KH instability could be measured at very limited viewing angles as demonstrated by three-dimensional simulation and forward modeling (Syntelis & Antolin 2019), so its occurrence could have been underestimated owing to projection effect. In order to assess the associated heating process and plasma acceleration as observed in this event, one may have to

do a three-dimensional simulation with a multifluid approach. Such events are reported in space plasmas (e.g. Moore et al. 2017); a dedicated review on KH instability and its secondary processes in space plasmas can be found in Masson & Nykyri (2018). In the solar corona, ion-scale processes would not be resolved with current instrumentation in the near future, but the secondary effects of MHD instabilities, such as plasma heating, particle acceleration, and mass and energy transportation, could manifest themselves in the macroscopic plasma parameters during MHD-scale observations.

ORCID iDs

Ding Yuan ⓘ https://orcid.org/0000-0002-9514-6402
Yuandeng Shen ⓘ https://orcid.org/0000-0001-9493-4418
Yu Liu ⓘ https://orcid.org/0000-0002-7694-2454
Hongbo Li ⓘ https://orcid.org/0000-0001-5649-6066
Xueshang Feng ⓘ https://orcid.org/0000-0001-8605-2159
Rony Keppens ⓘ https://orcid.org/0000-0003-3544-2733

References

Aschwanden, M. J., Boerner, P., Schrijver, C. J., & Malanushenko, A. 2013, SoPh, 283, 5
Berger, T., Hillier, A., & Liu, W. 2017, ApJ, 850, 60
Berné, O., Marcelino, N., & Cernicharo, J. 2010, Natur, 466, 947
Braginskii, S. I. 1965, RvPP, 1, 205
Bucciantini, N., Amato, E., & Del Zanna, L. 2005, A&A, 434, 189
Chandrasekhar, S. 1961, Hydrodynamic and Hydromagnetic Stability (New York: Dover)
De Pontieu, B., McIntosh, S. W., Carlsson, M., et al. 2011, Sci, 331, 55
Del Zanna, G., Dere, K. P., Young, P. R., Landi, E., & Mason, H. E. 2015, A&A, 582, A56
Fang, X., Yuan, D., Xia, C., Van Doorsselaere, T., & Keppens, R. 2016, ApJ, 833, 36
Feng, L., Inhester, B., & Gan, W. Q. 2013, ApJ, 774, 141
Foullon, C., Verwichte, E., Nakariakov, V. M., Nykyri, K., & Farrugia, C. J. 2011, ApJL, 729, L8
Freeland, S. L., & Handy, B. N. 1998, SoPh, 182, 497
Hannah, I. G., & Kontar, E. P. 2012, A&A, 539, A146
Hillier, A., & Polito, V. 2018, ApJL, 864, L10
Houze, R. A. 2014, in Cloud Dynamics, ed. R. A. Houze (New York: Academic), 25
Huang, G., Melnikov, V. F., Ji, H., & Ning, Z. 2018, Diagnostics of Flaring Loop Parameters (Singapore: Springer), 217
Johnson, J. R., Wing, S., & Delamere, P. A. 2014, SSRv, 184, 1
Klimchuk, J. A. 2006, SoPh, 234, 41
Lemen, J. R., Title, A. M., Akin, D. J., et al. 2012, SoPh, 275, 17
Li, D., Shen, Y., Ning, Z., Zhang, Q., & Zhou, T. 2018a, ApJ, 863, 192
Li, X., Zhang, J., Yang, S., Hou, Y., & Erdélyi, R. 2018b, NatSR, 8, 8136
Liu, Z., Xu, J., Gu, B.-Z., et al. 2014, RAA, 14, 705
Lobanov, A. P., & Zensus, J. A. 2001, Sci, 294, 128
Masson, A., & Nykyri, K. 2018, SSRv, 214, 71
Moore, T. W., Nykyri, K., & Dimmock, A. P. 2017, JGRA, 122, 128
Murray, S. D., White, S. D. M., Blondin, J. M., & Lin, D. N. C. 1993, ApJ, 407, 588
Ofman, L., & Thompson, B. J. 2011, ApJL, 734, L11
Ruan, W., Xia, C., & Keppens, R. 2018, A&A, 618, A135
Ryutova, M., Berger, T., Frank, Z., Tarbell, T., & Title, A. 2010, SoPh, 267, 75
Shen, Y., Liu, Y., Su, J., & Deng, Y. 2012, ApJ, 745, 164
Shen, Y., Liu, Y. D., Su, J., Qu, Z., & Tian, Z. 2017, ApJ, 851, 67
Smyth, W. D., & Moum, J. N. 2012, Oceanography, 25, 140
Sterling, A. C., Moore, R. L., Falconer, D. A., & Adams, M. 2015, Natur, 523, 437
Syntelis, P., & Antolin, P. 2019, ApJL, 884, L4
Thomson, W. (Lord Kelvin). 1871, PMag, 42, 362
Vietri, M., Ferrara, A., & Miniati, F. 1997, ApJ, 483, 262
von Helmholtz, H. 1868, Berl. Monatsber., 23, 215
Wang, C.-Y., & Chevalier, R. A. 2001, ApJ, 549, 1119
Yang, H., Xu, Z., Lim, E.-K., et al. 2018, ApJ, 857, 115